

# Molybdenum Trioxide on Anatase $\text{TiO}_2(101)$ - Formation of Monodispersed $(\text{MoO}_3)_1$ Monomers from Oligomeric $(\text{MoO}_3)_n$ Clusters

*Nassar Doudin,<sup>†, #, ‡</sup> Gregory Collinge,<sup>†, †</sup> Pradeep Kumar Gurunathan,<sup>†</sup> Mal-Soon Lee,<sup>†</sup> Vassiliki-Alexandra Glezakou,<sup>†</sup> Roger Rousseau,<sup>†, \*</sup> Zdenek Dohnálek<sup>†, ‡, \*</sup>*

<sup>†</sup> Physical and Computational Sciences Directorate and Institute for Integrated Catalysis, Pacific Northwest National Laboratory, P.O. Box 999, Richland, Washington 99352, United States

<sup>‡</sup> Voiland School of Chemical Engineering and Bioengineering, Washington State University, Pullman, Washington 99163, United States

<sup>#</sup> Present address: Department of Chemical & Environmental Engineering, Yale University, New Haven, Connecticut 06437, United States

<sup>†</sup> These authors contributed equally

\* Corresponding authors: RR email: [roger.rousseau@pnnl.gov](mailto:roger.rousseau@pnnl.gov), ZD email:

[Zdenek.Dohnalek@pnnl.gov](mailto:Zdenek.Dohnalek@pnnl.gov)

## ABSTRACT

Complex oxide systems with hierarchical order are of critical importance in material science and catalysis. Despite their immense potential, their design and synthesis are rather difficult. In this study we demonstrate how the deposition of small oligomeric  $(\text{MoO}_3)_{1-6}$  clusters, which can be formed by the sublimation of  $\text{MoO}_3$  powders, leads to the formation of locally ordered layers of  $(\text{MoO}_3)_1$  monomers on anatase  $\text{TiO}_2(101)$ . Using both high-resolution imaging and theoretical calculations, we show that at room temperature, such oligomers undergo spontaneous dissociation to their monomeric units. In initial stages of the deposition, this is reflected by the observation of one to six neighboring  $(\text{MoO}_3)_1$  monomers that parallel the size distribution of the oligomers. A transient mobility of such oligomers on both bare  $\text{TiO}_2(101)$  and  $(\text{MoO}_3)_1$  covered areas is key to the formation of a complete layer with a saturation coverage of one  $(\text{MoO}_3)_1$  per two undercoordinated surface Ti sites. We further show that such layers are stable to 500 K, making them highly suitable for a broad range of applications.

## 1. INTRODUCTION

Oxide clusters supported on oxide substrates are of great interest due to their importance in materials science and heterogeneous catalysis.<sup>1-5</sup> The nature and strength of their interactions not only determine their structure, distribution, and stability but ultimately also their overall activity.<sup>6-</sup><sup>8</sup> Understanding their interactions at an atomistic level is, therefore, critical to tailoring oxide on oxide systems to achieve the desired properties and activity. For example, in materials science, the self-assembly of oxides into ordered structural motifs is one of the critical challenges for the design of hierarchical materials,<sup>9-12</sup> and in catalysis, the activity often depends on the dispersion and binding configurations of the supported oxide clusters.<sup>2, 13-14</sup>

Titanium dioxide, employed here, is a versatile oxide material with important applications in many areas.<sup>15-16</sup> It is often used as a model reducible oxide, and as such, understanding factors that control the growth and aggregation of metal oxide clusters are of fundamental importance. Moreover, the underlying principles can provide the guidance necessary to understand how to prepare clusters of the desired size that would allow us to explore the relation between cluster size and activity.<sup>14, 17-19</sup>

In contrast, studies of metal oxide clusters on well-defined anatase surfaces are scarce.<sup>6, 20</sup> Aside from its role as support for MoO<sub>3</sub>-based thermocatalysts, anatase is of particular interest in photocatalysis,<sup>21-22</sup> where oxide clusters (such as clusters of WO<sub>3</sub> and MoO<sub>3</sub>) may be employed to enhance its photocatalytic efficiency and activity.<sup>23-27</sup>

Our specific interest in TiO<sub>2</sub>-supported MoO<sub>3</sub> is primarily derived from its ability to act as both a Lewis acid and base, and as a redox-active promoter. In this respect, this work connects directly to our prior studies of the cyclic (WO<sub>3</sub>)<sub>3</sub> trimers on rutile TiO<sub>2</sub>(110) and other substrates.<sup>2, 8, 17, 28-</sup><sup>29</sup> In these studies, we focused on understanding how the binding of such clusters affects the

competition between catalytic dehydration, dehydrogenation, and condensation of alcohols as model reactions.<sup>2, 8, 17, 28-29</sup> The acid/base properties of TiO<sub>2</sub>-supported MoO<sub>3</sub> were demonstrated in 1975 via NH<sub>3</sub> and CO<sub>2</sub> titration methods by Mamoru<sup>29</sup> while the redox activity of TiO<sub>2</sub>-supported MoO<sub>3</sub> was probed by electron paramagnetic resonance during butadiene oxidation by Akimoto *et al* in 1973.<sup>31</sup> Other studies have consistently shown the acidity/basicity<sup>32-33</sup> and redox activity<sup>34-36</sup> of this material since then, and some researchers have additionally focused on the dispersive and agglomeration resistant properties of TiO<sub>2</sub>-supported MoO<sub>3</sub>, as well.<sup>32, 37</sup> From these studies, it is clear that TiO<sub>2</sub>-supported MoO<sub>3</sub> possesses many properties that deem it a promising catalytic material for a large variety of applications.

From a computational standpoint, many studies have been carried out to elucidate the structure, reducibility and stability of supported molybdenum oxide clusters.<sup>38-45</sup> However, relatively few computational studies have dealt with the issue of molybdenum oxide clusters supported on TiO<sub>2</sub>. During the last decade, Paul and co-workers investigated the structure of MoO<sub>3</sub> and Mo<sub>2</sub>O<sub>6</sub> species on anatase TiO<sub>2</sub>(101).<sup>43-44</sup> They found that the “distorted tetrahedral” mono-oxo species is the most stable monomeric (MoO<sub>3</sub>)<sub>1</sub> structure, which is largely in agreement with the results presented here. At around the same time, Kim *et al.* showed similar results for MoO<sub>3</sub> on rutile TiO<sub>2</sub>(110).<sup>45</sup>

In this study, we follow the deposition of well-defined small (MoO<sub>3</sub>)<sub>n</sub> oligomers ( $n = 1-6$ )<sup>2, 46</sup> on anatase TiO<sub>2</sub>(101) surface. Using high-resolution imaging via scanning tunneling microscopy (STM), spectroscopic characterization by X-ray photoelectron spectroscopy (XPS), deposited mass quartz measurements with crystal microbalance (QCM), and with theoretical studies via density functional theory (DFT) we find that at 295 K the (MoO<sub>3</sub>)<sub>1-6</sub> oligomers fall apart into (MoO<sub>3</sub>)<sub>1</sub> monomeric units with all Mo ions being in the (6+) oxidation state. The (MoO<sub>3</sub>)<sub>1</sub> monomers from each oligomer remain in close proximity forming groupings that at low coverages

reflect the distribution of gas phase  $(\text{MoO}_3)_n$  oligomers. The higher stability of  $(\text{MoO}_3)_1$  is confirmed by DFT and a conceivable, low-energy dissociation path is derived. At intermediate coverages, the groupings increase in size, indicating that the  $(\text{MoO}_3)_n$  oligomers are transiently mobile before they fall apart. Ultimately, due to such mobility, a complete layer with relatively high order of  $(\text{MoO}_3)_1$  can be prepared. At all coverages, the  $(\text{MoO}_3)_1$  overlayers exhibit thermal stability all the way to  $\sim 500$  K, where the onset of reduction and disordering is observed. This work demonstrates a simple and generalizable method for the preparation of complex hierarchical oxides.

## 2. RESULTS AND DISCUSSION

**Cluster Deposition and Dissociation at Room Temperature.** As outlined in the Introduction above and Experimental Methods sections, the sublimation of  $\text{MoO}_3$  powders leads to the formation of gas-phase oligomeric  $(\text{MoO}_3)_n$  clusters ( $n = 1-6$ ), with the distribution dominated by  $(\text{MoO}_3)_3$ . This cluster size distribution was determined previously using IRAS spectroscopy<sup>46</sup> but has not been confirmed via a direct high-resolution STM imaging. The results of such experiments on anatase  $\text{TiO}_2(101)$  are presented in Figure 1.

The images shown in Figure 1a and b illustrate the clean anatase  $\text{TiO}_2(101)$  surface prior to the molybdenum trioxide deposition. The imaged surface (Figure 1a) displays large terraces with a trapezoidal shape that are separated by  $3.8 \text{ \AA}$  high monoatomic steps.<sup>47-48</sup> The atomic surface structure is schematically shown using a ball-and-stick model in the inset of Figure 1b. The terraces have a sawtooth corrugation composed of fully coordinated, 6-fold coordinated titanium atoms ( $\text{Ti}_{6c}$ ) and 3-fold coordinated oxygen atoms ( $\text{O}_{3c}$ ), as well as under-coordinated, 5-fold coordinated titanium atoms ( $\text{Ti}_{5c}$ ) and 2-fold coordinated oxygen atoms ( $\text{O}_{2c}$ ). The high-resolution empty-state STM image (Figure 1b), shows the rows of bright oval-shaped features along the  $[010]$  direction

originating both from the  $O_{2c}$ , (red dots) and  $Ti_{5c}$  (blue dots).<sup>49</sup> Generally, the  $TiO_2(101)$  surface is non-reconstructed and exhibits low concentration of point defects with oxygen vacancy defects residing in the subsurface region.<sup>15, 49-50</sup> This is reflected in our STM images (Figure 1a-b) where only a few atomically sized imperfections can be observed, even after the sample is left in vacuum at room temperature for several days.

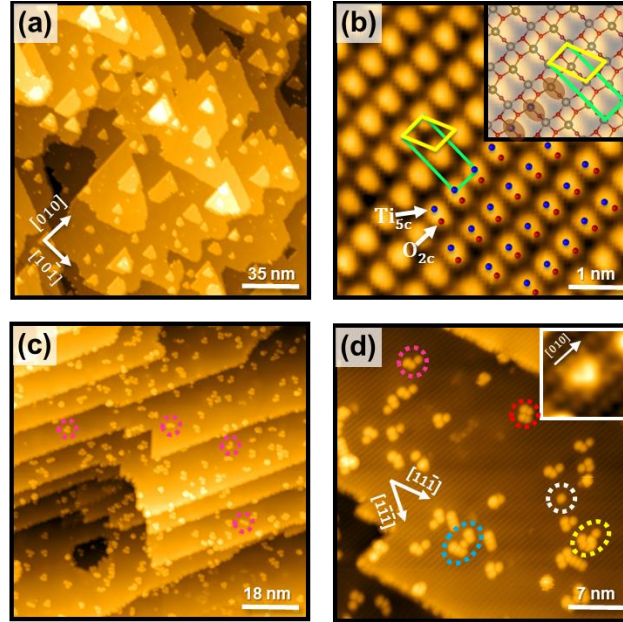


**Figure 1.** (a) The large scale STM image of clean anatase  $TiO_2(101)$  ( $175 \times 175 \text{ nm}^2$ , sample bias,  $V_s = +1.2 \text{ V}$ , tunneling current,  $I_t = 60 \text{ pA}$ ). (b) High-resolution STM image ( $5 \times 5 \text{ nm}^2$ ,  $V_s = +0.9 \text{ V}$ ,  $I_t = 120 \text{ pA}$ ) of  $TiO_2(101)$ . The approximate positions of  $O_{2c}$  and  $Ti_{5c}$  atoms is marked by red and blue dots, respectively. The inset in (b) represents a ball-and-stick top view of the surface. Red and purple spheres represent  $O_{3c}$  and  $O_{2c}$ , respectively, dark and light gray spheres represent  $Ti_{6c}$  and  $Ti_{5c}$ , respectively. The rectangular surface unit cell ( $10.24 \text{ \AA} \times 3.78 \text{ \AA}$ , DFT:  $10.46 \text{ \AA} \times 3.83 \text{ \AA}$ )<sup>50</sup> and primitive unit cells are marked in green and yellow, respectively. (c) Large-scale STM images ( $100 \times 100 \text{ nm}^2$ ,  $V_s = 1.9 \text{ V}$ ,  $I_t = 40 \text{ pA}$ ) after the deposition of 0.03 monolayer (ML) of  $(MoO_3)_1$  equivalents at 295 K. Here 1 ML is defined relative to the coverage of  $Ti_{5c}$  atoms. Several groupings of three neighboring bright features typically observed at low coverages are highlighted by the dotted pink circles. (d) High-resolution STM image ( $35 \times 35 \text{ nm}^2$ ,  $V_s = +1.3 \text{ V}$ ,  $I_t = 80 \text{ pA}$ ) after the deposition of 0.03 ML of  $(MoO_3)_1$  equivalents at 295 K. Several clusters with one, three, four, five, and six bright spots are highlighted by white, pink, red, yellow, and cyan ellipses. The inset in (d) shows a high-resolution STM image ( $3 \times 3 \text{ nm}^2$ ,  $V_s = 1.0 \text{ V}$ ,  $I_t = 80 \text{ pA}$ ) of a single isolated bright feature such as the one highlighted with the white circle in (d).

STM images acquired after the deposition of a small amount of molybdenum trioxide (0.03 ML of  $(\text{MoO}_3)_1$  equivalents) onto  $\text{TiO}_2(101)$  at 295 K are shown in Figure 1c and d. Following the deposition, new bright features with identical appearance and symmetry are distributed across the surfaces. The diameter of each feature is  $\sim 5.8 \text{ \AA}$ , and the apparent height is  $\sim 1.2 \text{ \AA}$ . Although the bright features are most often observed in clusters of threes (pink ovals, Figure 1c and d), small fractions of single (white), four (red), five (yellow), and six (cyan) bright features can also be seen. The statistical analysis of the number of neighboring bright features from several large scale STM images such as the ones shown in Figure 1c and d yields a distribution of 9%, 6%, 60%, 7%, 2%, and 12% for clusters of 1, 2, 3, 4, 5, and 6 bright features as displayed in Figure 2a (black bars). This distribution is rather similar to the distribution of cyclic  $(\text{MoO}_3)_{3-6}$  clusters (gray bars, Figure 2a) determined previously from the IRAS spectra of the  $(\text{MoO}_3)_n$  clusters isolated in a Kr matrix.<sup>46</sup> There, the breathing modes of cyclic clusters between  $800$  and  $900 \text{ cm}^{-1}$  were used to determine the population of 61%, 17%, 15%, and 7% for trimers, tetramers, pentamers, and hexamers, respectively. This similarity between the distributions of neighboring bright spots in the STM and the population of  $(\text{MoO}_3)_n$  clusters in IRAS suggests that the neighboring bright spots originate from a single deposited  $(\text{MoO}_3)_n$  (e.g., three bright spots originate from a single  $(\text{MoO}_3)_3$ ). Since the distances between the bright spots are too large to come from an intact  $(\text{MoO}_3)_n$  we assert that the clusters fall apart on the  $\text{TiO}_2(101)$  and that each bright feature corresponds to  $(\text{MoO}_3)_1$  monomer.

Additionally the Mo 3d X-ray photoelectron spectroscopy (XPS) spectra (Section S1, Supporting Information) show that all Mo is in (6+) oxidation state.<sup>28</sup> Only two peaks due to Mo  $3d_{3/2}$  and Mo  $3d_{5/2}$  are observed at 235.5 and 232.3 eV. This suggests that there is only one type of

Mo cations in the deposited molybdenum oxide; i.e., all Mo atoms have the same chemical surrounding and bonding configuration. This is further evidence that the  $(\text{MoO}_3)_3$  falls apart into three identical  $(\text{MoO}_3)_1$  monomers.

To confirm the assertion that each bright spot in the STM corresponds to  $(\text{MoO}_3)_1$ , we determined the absolute amount of deposited  $(\text{MoO}_3)_1$  equivalents from Quartz crystal microbalance (QCM) and XPS measurements (Figure 2b). In the QCM experiments, the areal density of  $(\text{MoO}_3)_1$  was determined from the weight of molybdenum trioxide deposited on the QCM sensor in the same position as that used for the deposition on the sample. This density was subsequently correlated with the density of bright features in the STM as a function of deposition time. The results of this correlation are shown as blue squares in Figure 2b. The slope (blue dotted line) of this correlation is very close to unity ( $0.95 \pm 0.03$ ), showing that each bright feature in the STM corresponds to  $(\text{MoO}_3)_1$  monomer.

A similar correlation is obtained from the take-off angle-dependent XPS analysis (see Section S2, Supporting Information) that is displayed as red squares in Figure 2b. The slope is also very close to unity ( $1.04 \pm 0.03$ ) confirming our assignment. Overall, the combined STM, XPS, and QCM analysis reveals that the gas phase  $(\text{MoO}_3)_n$  clusters readily decompose at 295 K into monomeric  $(\text{MoO}_3)_1$  units.



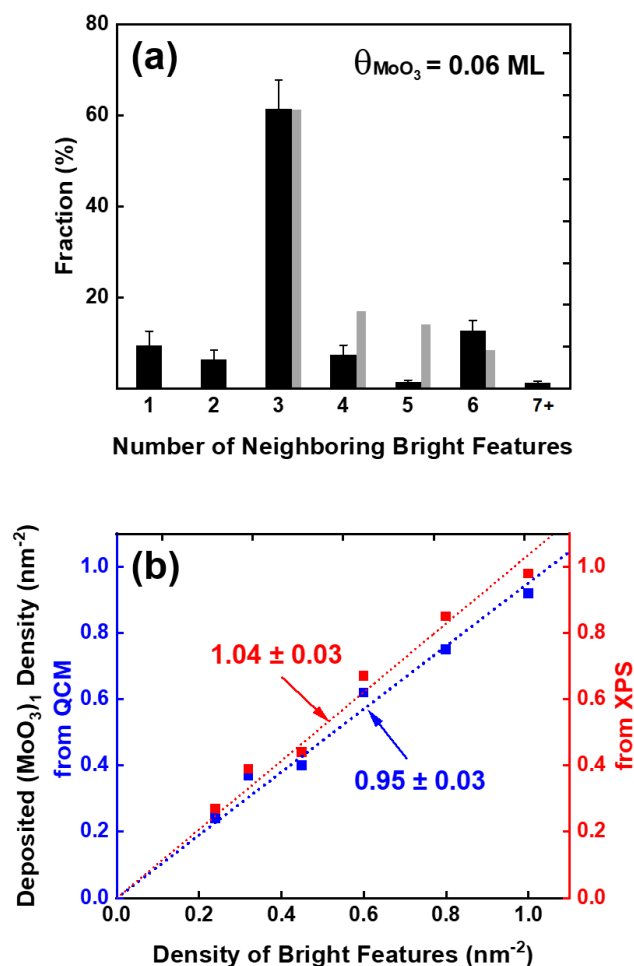


**Figure 2.** (a) Fractional population of the groupings of bright features with a different number of neighbors observed in STM following the deposition of 0.03 ML  $(\text{MoO}_3)_1$  equivalents on anatase  $\text{TiO}_2(101)$  at 295 K. (b) Correlation of the  $(\text{MoO}_3)_1$  areal density deposited per unit area from QCM (blue) and XPS (red) measurements with the density of bright features per unit area in the STM images. The dotted lines are the linear least-square fits to the data and yield the number of  $\text{MoO}_3$  units in each bright feature.

Density functional theory (DFT) calculations are further employed to assess the thermodynamic driving force for the dissociation of adsorbed  $(\text{MoO}_3)_n$  clusters. The most abundant cyclic  $(\text{MoO}_3)_3$  is chosen as a model for the calculations. We have carried out an extensive search for the most stable binding configuration of  $(\text{MoO}_3)_3$  (Section S3, Supplementary Information) using a smaller  $(4 \times 6)$  surface cell—corresponding to a  $(\text{MoO}_3)_3$  coverage of 0.042 ML or  $\sim 0.10 (\text{MoO}_3)_3/\text{nm}^2$ . Following the initial screening, we have carried out additional calculations on a larger  $(6 \times 8)$

surface cell ( $\sim 0.021$  ML or  $\sim 0.05$  (MoO<sub>3</sub>)<sub>3</sub>/nm<sup>2</sup>) for the energetically most favorable configurations that are shown in Figure 3. The most stable adsorption configuration for (MoO<sub>3</sub>)<sub>3</sub> (Figure 3a) is found to bind with an adsorption energy of -529 kJ/mol/(MoO<sub>3</sub>)<sub>3</sub> or -176 kJ/mol/(MoO<sub>3</sub>)<sub>1</sub> in the larger surface cell (revealing notable repulsive interactions in the smaller surface cell, see Figure S3). In the most stable (MoO<sub>3</sub>)<sub>3</sub> configuration, one terminal Mo=O group on each Mo(VI) is bound to three different Ti<sub>5c</sub> sites, leaving the second Mo=O group on each Mo(VI) pointing into the vacuum and the remainder O bridging Mo atoms. It is interesting to note that binding energy of the second most favorable configuration is only 3% less stable (5 kJ/mol/(MoO<sub>3</sub>)<sub>1</sub> difference, see Figure S3e and f, Supplementary Information) where the cluster is rotated on the surface  $\sim 180^\circ$  relative to the most stable configuration. This underscores the fact that the potential energy surface may contain many similar minima.

The two most stable structures for an isolated (MoO<sub>3</sub>)<sub>1</sub> monomer are shown in Figure 3b-c. In both structures, two (MoO<sub>3</sub>)<sub>1</sub> oxygens are bound to two Ti<sub>5c</sub> sites in the same row, while the Mo(VI) is bound to one O<sub>2c</sub> oxygen of TiO<sub>2</sub> in the (MoO<sub>3</sub>)<sub>1</sub> monomer shown in Figure 3b and to two O<sub>2c</sub> oxygens of TiO<sub>2</sub> in the (MoO<sub>3</sub>)<sub>1</sub> monomer shown in Figure 3c. In both structures, one Mo=O functional group remains free and pointing away from the surface, making the most stable (MoO<sub>3</sub>)<sub>1</sub> monomers mono-oxo species. Their calculated adsorption energies of -227 kJ/mol/(MoO<sub>3</sub>)<sub>1</sub> and -223 kJ/mol/(MoO<sub>3</sub>)<sub>1</sub> are significantly stronger than that of (MoO<sub>3</sub>)<sub>3</sub>. Combined with an obvious entropic driving force (1 (MoO<sub>3</sub>)<sub>3</sub> converting to 3 (MoO<sub>3</sub>)<sub>1</sub>), we conclude that the dissociation process is heavily exergonic regardless of which monomer is created. It is worth noting that the most stable (MoO<sub>3</sub>)<sub>1</sub> structure we have identified here is the same as that found by Paul and co-workers using a purely GGA functional (i.e., without dispersion or correlation corrections).<sup>43-44</sup> Additionally, despite the different surface, the MoO<sub>3</sub> structure on

rutile  $\text{TiO}_2(110)$  found by Metiu and co-workers<sup>45</sup> is also nearly identical, displaying the same coordination environment as the monomer shown in Figure 3c (two  $\text{Mo-O}_{2c}$  and two  $\text{O-Ti}_{5c}$  bonds, a single  $\text{Mo=O}$ ). While the  $(\text{MoO}_3)_1$  monomer shown in Figure 3b has slightly stronger adsorption energy (by  $\sim 5 \text{ kJ/mol}/(\text{MoO}_3)_1$ ) than the  $(\text{MoO}_3)_1$  monomer shown in Figure 3c, the two are well within typically cited DFT errors and thus should be regarded as essentially isoenergetic. Other  $(\text{MoO}_3)_1$  adsorption configurations that we explored (from an extensive search on the  $(6\times 8)$  surface cell) are significantly less stable di-oxo species and are shown in Section S4 of the Supplementary Information.

To further facilitate the comparison of the theory with the experiment, we have simulated empty-state STM images that correspond to the structures of adsorbed  $(\text{MoO}_3)_3$  and the two contending  $(\text{MoO}_3)_1$  that are shown in Figure 3. While the simulated  $(\text{MoO}_3)_3$  image is somewhat larger than that of the two  $(\text{MoO}_3)_1$  monomers, their spatial appearance is rather similar, with one brighter maximum along  $[10\bar{1}]$  direction and two fainter maxima along the  $[010]$  direction. From the spatial extent of the images, one can conclude that both Mo(VI) and terminal O of the  $\text{Mo=O}$  functional groups are being imaged. Overall, even though a simple visual comparison (Figure 1d, inset) does not yield a definitive assignment, a comparison of the measured and simulated dimensions of each bright species strongly suggests that the bright spots are *not* the trimer structure shown in Figure 3a. As mentioned previously, the apparent width of the bright features in the high-resolution STM images is  $\sim 5.8 \text{ \AA}$ , while the width of the simulated trimer STM images shown in Figure 3a-iii (along the  $[10\bar{1}]$  direction) is  $\sim 8.9 \text{ \AA}$ . The two simulated monomer STM images appear to have the same dimension of  $\sim 5.9 \text{ \AA}$  as shown in Figure 3b-iii and Figure 3c-iii. Unfortunately, a conclusive assignment of the monomer to the bright features seen in the high-resolution STM images (Figure 1) is not possible based on the available experimental and computational evidence.

Nonetheless, we have chosen to perform further calculations using the  $(\text{MoO}_3)_1$  monomer shown in Figure 3c (despite its negligibly weaker adsorption energy) because it appears to display the same orientation to the  $\text{TiO}_2$  surface as that seen in the high-resolution STM images (Figure 1d, inset), with the brightest maxima pointing in the positive  $[10\bar{1}]$  direction instead of in the negative  $[10\bar{1}]$  direction (as defined in Figure 1 and Figure 3).

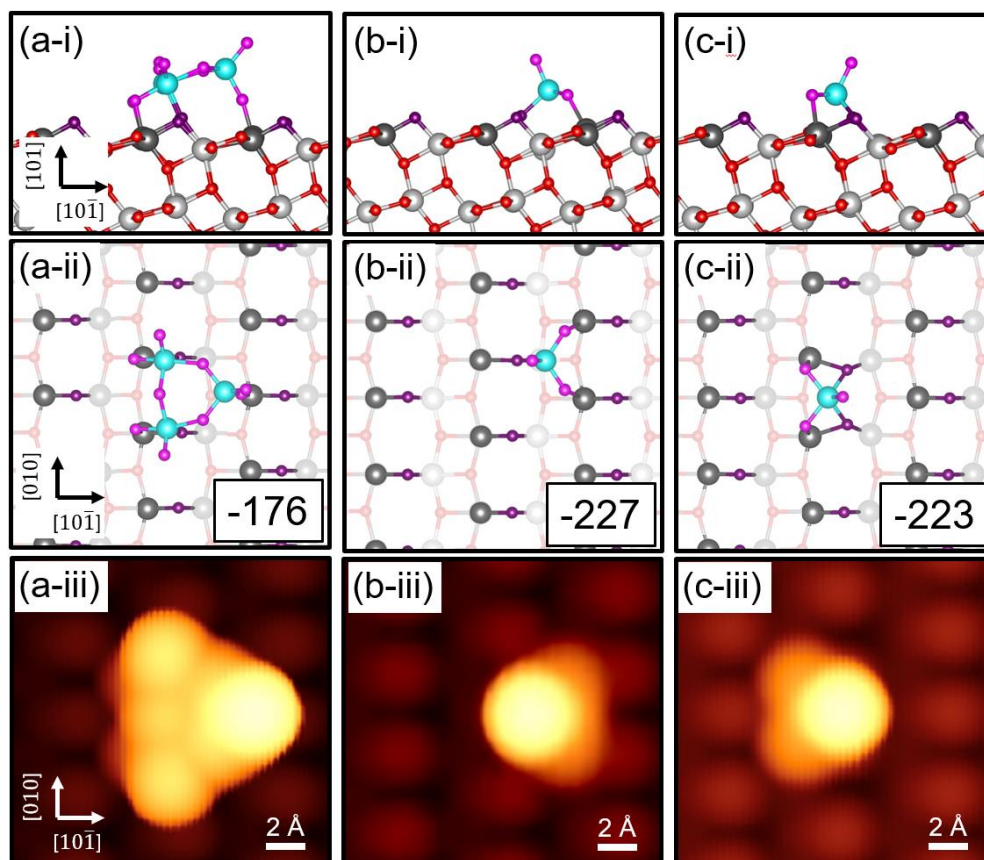


**Figure 3.** Most stable adsorption configurations for (a) cyclic  $(\text{MoO}_3)_3$  trimer and (b)  $(\text{MoO}_3)_1$  monomer on  $\text{TiO}_2(101)$  as determined by DFT. Side (i) and top (ii) views of the ball and stick models. Corresponding adsorption energies (in  $\text{kJ/mol}/(\text{MoO}_3)_1$ ) are shown in (ii). The simulated STM ( $V_s = +3.0$  V) images for each structure are shown in (iii). Anatase  $\text{TiO}_2(101)$  atoms: Light gray represents  $\text{Ti}_{6c}$ , dark gray  $\text{Ti}_{5c}$ , red  $\text{O}_{3c}$ , and purple  $\text{O}_{2c}$ .  $\text{MoO}_3$  atoms: turquoise are Mo and magenta O.

With the strong evidence for  $(\text{MoO}_3)_3$  dissociation and higher stability of  $(\text{MoO}_3)_1$  species provided above, a natural question is how such a multistep process proceeds and what the rate-limiting steps are. To accomplish this, we first follow the areal distribution of the resulting three  $(\text{MoO}_3)_1$  monomers (“trios”). Experimentally we find that the neighboring monomers are always distributed on at least two  $\text{Ti}_{5c}$  rows. The four observed configurations are summarized in the high-magnification STM image and the corresponding structural models from DFT in Figure 4a. Two configurations span three neighboring rows and we term them linear cross-row trios (aligned) (LCT) and bent triangular trios (BTT) with directions between the neighboring monomers along  $[11\bar{1}]$  or  $[1\bar{1}\bar{1}]$  directions. The other two configurations span only two neighboring rows with two of the monomers along  $[010]$  direction and the third in the adjacent row. We term them acute triangular trios (ATT) and obtuse triangular trios (OTT). The energies of all four configurations (see Figure 4a) are within 5 kJ/mol/ $(\text{MoO}_3)_1$  (197-192 kJ/mol/ $(\text{MoO}_3)_1$ ). The statistical evaluation of the STM images (Figure 4b) shows that the observed populations are also identical within the error of the analysis. We have simulated the STM image for the ATT configuration and the result can be found in Section S5 of the Supporting Information.

Interestingly the fifth possible configuration, with all monomers on the same  $\text{Ti}_{5c}$  row, a linear along-row trio (LAT, Figure 4a), is never observed in the STM. The DFT calculations show that the adsorption energy of this configuration is somewhat lower (186 kJ/ $(\text{MoO}_3)_1$ ) than the other ones such that a Boltzmann weighted population would be about ~3% at 295 K making it unlikely to be observed (this value accounts for the degenerate configurations of the other trios). In addition, the LAT configuration places the monomers at the ends of the trio closer to each other’s images due to the limited size of the DFT slab than do the other configurations. Thus, it is very likely that the LAT configuration experiences greater electrostatic repulsions that would reduce its binding

strength. We speculate, therefore, that the true isolated LAT binding energy is in fact comparable to the other configurations, making it thermodynamically just as favorable. We thus conclude that the first step of the  $(\text{MoO}_3)_3$  unfolding and dissociation has to occur across the two neighboring  $\text{Ti}_{5c}$  rows which would explain the absence of the LAT configuration.

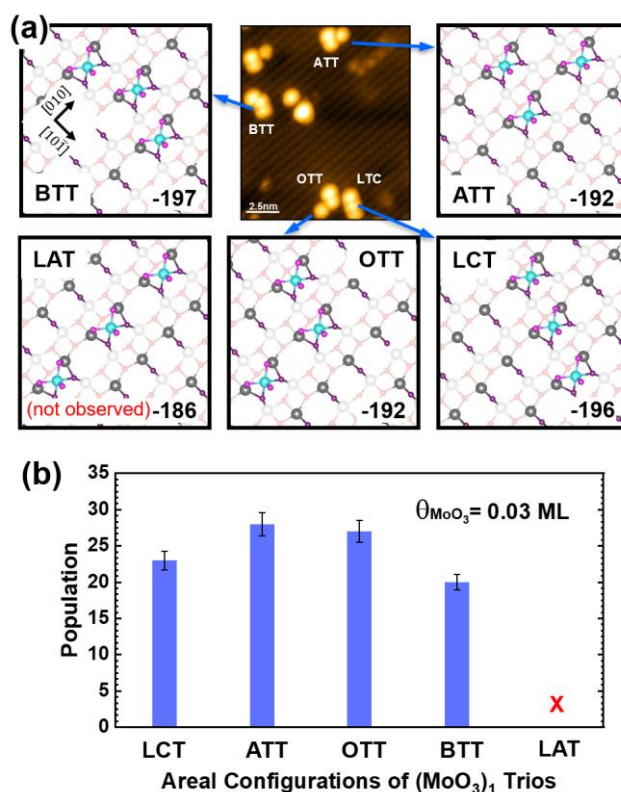


**Figure 4.** (a) High-magnification STM image illustrating the four experimentally observed configurations of three neighboring  $(\text{MoO}_3)_1$  monomers (trios) resulting from the  $(\text{MoO}_3)_3$  dissociation on anatase  $\text{TiO}_2(101)$ . The corresponding ball and stick models show the corresponding structures and their adsorption energies as determined by DFT. The acronyms for the configurations refer to linear cross-row trio (LCT), bent triangular trio (BTT), acute triangular trio (ATT), and obtuse triangular trio (OTT). The fifth, configuration labeled linear along-row trio (LAT) is not observed experimentally. (b) The population of LCT, BTT, ATT, OTT, and LAT configurations determined from STM images after the deposition of molybdenum trioxide at 295 K. The distributions were evaluated in five  $100 \times 100 \text{ nm}^2$  STM images from the same experiment.

As seen in Figure 5, this conclusion is supported by DFT calculations showing dissociation of the cyclic  $(\text{MoO}_3)_3$  proceeds via a multistep pathway in which the  $(\text{MoO}_3)_3$  ring indeed opens and unfolds, as its first step, across (or nearly across) the two  $\text{Ti}_{5c}$  rows that the trimer initially sits

between (see the rows of dark grey  $\text{Ti}_{5c}$  spheres running along the [010] direction in Figure 5a). This pathway was revealed by continuing to run AIMD in the NVT ensemble for an additional 1.5 ps past the initial  $\sim 10$  ps to ensure that the lowest energy conformation of  $(\text{MoO}_3)_3$  was found. At an increased temperature of 2000 K to accelerate the decomposition process, 1.5 ps was all that was needed to accomplish complete decomposition. This strategy allowed us to identify which bonds are most likely to break as  $(\text{MoO}_3)_3$  spontaneously dissociates along the MD trajectory and to then replicate the trajectory as a CINEB. We also note that in this process there is an active involvement of the surface which deforms along with the cluster to facilitate bond breaking: a fact which would make a simulation via NEB, without the input from the short AIMD trajectory, unlikely to yield low decomposition barriers. This method proved to be essential to acquiring the results presented in Figure 5. While extensive attempts were made to find other possible pathways, none could be identified beyond those revealed during AIMD—all alternatives explored exhibit prohibitively high reaction barriers ( $> 100$  kJ/mol). However, we note that the phase space of this system is large, and it is likely that other pathways for  $(\text{MoO}_3)_3$  decomposition are possible.

The  $(\text{MoO}_3)_3$  decomposition pathways in Figure 5 exhibits nine total stationary states according to the CINEB method employed. The constituent  $(\text{MoO}_3)_1$  units of the  $(\text{MoO}_3)_3$  trimer are labeled as constituent monomers (CM) “1”, “2”, and “3” in Figure 5a to aid the discussion. Each step within the pathway appears to be driven by the creation of new  $\text{Ti}_{5c}$ -O bonds. As mentioned above, the first step, (a) – (b), involves ring opening of cyclic  $(\text{MoO}_3)_3$  to form an open  $(\text{MoO}_3)_3$  trimer where the free Mo=O oxygen of CM #1 is able to coordinate to an additional  $\text{Ti}_{5c}$ . As seen in steps (b) – (c), CM #1 then encroaches into the space of monomer #2 in order to form a  $\text{Ti}-\text{O}_{2c}$  bond and fully break from the open trimer (see the  $(\text{MoO}_3)_2 + (\text{MoO}_3)_1$  configuration in Figure 5c). From there, in steps (c) – (e), the  $(\text{MoO}_3)_2$  dimer reorients and re-bonds with CM#1 in order to form a

new and very stable open  $(\text{MoO}_3)_3$  trimer (calculated adsorption energy of  $-200 \text{ kJ/mol}/(\text{MoO}_3)_1$ ). However, based on visual inspections of the AIMD trajectory that the decomposition pathway is derived from, steps (c) – (e) should be regarded as largely approximate as its structures do not replicate those seen along the AIMD trajectory as well as the other steps shown here do. This is due to the tendency of the 0 K CINEB method to smooth out motion perpendicular to the reaction coordinate, which here effectively decouples the decomposition steps from the dynamic modes of the substrate induced at finite temperatures. Once the structure seen in Figure 5f is formed, the pathways more faithfully follows the AIMD trajectory. In these steps, (f) – (i), the newly formed open  $(\text{MoO}_3)_3$  trimer (structure (e)) rapidly decomposes into three monomeric  $(\text{MoO}_3)_1$  units. According to the results shown in the graph of the reaction pathways in Figure 5, structure (e) is calculated to be essentially isoenergetic with the final decomposed state (structure (i) in Figure 5), exhibiting an effective decomposition barrier of  $\sim 92 \text{ kJ/mol}/(\text{MoO}_3)_3$ . Such a barrier should be surmountable at modest temperatures ( $\geq 297 \text{ K}$ ). The estimated temperature is based on simple first order kinetics calculations to achieve experimentally observable decomposition/reassociation rates ( $\sim 10^{-3}$  turnovers/s) with a standard prefactor of  $10^{13} \text{ s}^{-1}$ .

By itself, the above analysis would indicate that the population of fully decomposed  $(\text{MoO}_3)_1$  monomers should be roughly equal to the population of open  $(\text{MoO}_3)_3$  trimers in the form of structure (e) with perhaps a minor contribution coming from structure (d). This could indicate that other decomposition pathways are more favorable to decomposition than the one found here. However, the most likely reason for the seeming discrepancy is the absence of thermal effects and collective dynamics from the pathways shown in Figure 5 since the cyclic  $(\text{MoO}_3)_3$  trimer was shown to rapidly decompose to structure (g) within our (accelerated) AIMD simulations in a remarkably short amount of simulated time (10 ps to get to structure (c) at 1000 K; only  $\sim 1.5$  ps



to proceed to structure (g) at 2000 K). Therefore, we posit that this is indeed a reasonable decomposition pathway for cycle  $(\text{MoO}_3)_3$ , overall consistent with the experimental evidence when paired with the corresponding AIMD simulations. The AIMD trajectories can be found in Section S6 of the Supplementary Information.

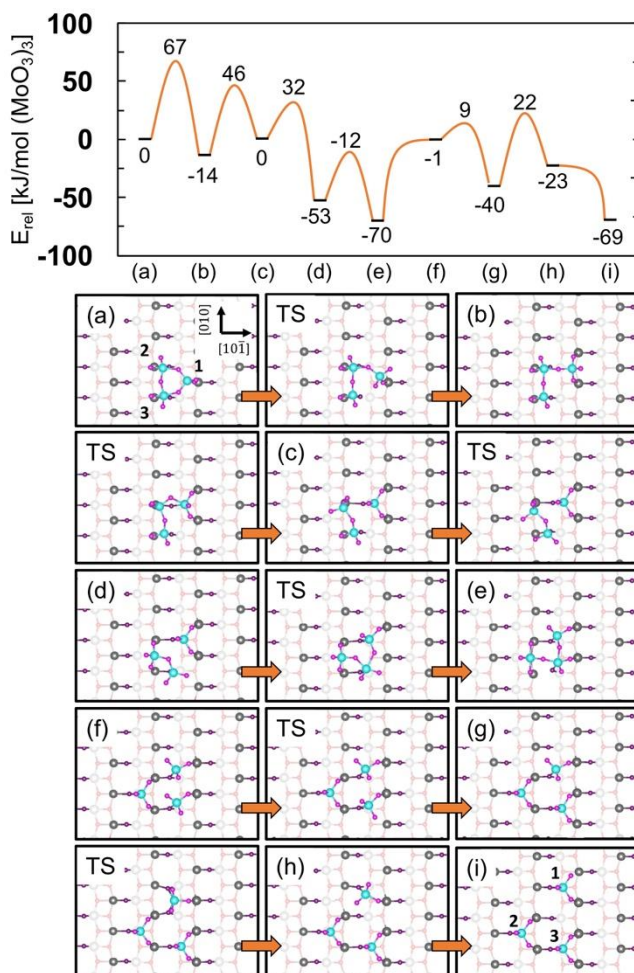


**Figure 5.**  $(\text{MoO}_3)_3$  decomposition pathways as determined by AIMD and the CINEB method. Stationary states are denoted as (a) through (i) while all transition states (between two subsequent stationary states) are denoted as “TS”. Color coding is the same as that used in Figure 3 and Figure 4.

**The electronic properties of adsorbed molybdenum trioxide.** As already discussed, we find that all Mo atoms are in the (6+) oxidation state. To complete the analysis of the electronic structure of molybdenum trioxide on  $\text{TiO}_2(101)$ , we calculated the projected densities of states (pDOS) as

shown in Figure 6 for the following scenarios: (a) gas phase  $(\text{MoO}_3)_3$  and bare  $\text{TiO}_2(101)$  in their equilibrium geometries; (b) spatially separated  $(\text{MoO}_3)_3$  and bare  $\text{TiO}_2(101)$  in distorted geometries that correspond to their conformations when adsorbed; (c) cyclic  $(\text{MoO}_3)_3$  trimer adsorbed on  $\text{TiO}_2(101)$  as schematically shown in Figure 3a; and (d) three  $(\text{MoO}_3)_1$  monomers that result from the dissociation of  $(\text{MoO}_3)_3$  (Figure 4a, ATT configuration). The presented pDOS are decomposed into local DOS contributions from the oxygen and titanium of  $\text{TiO}_2(101)$  (red and gray lines, respectively) and local DOS contributions from the oxygen and molybdenum of the molybdenum trioxide (magenta and cyan lines, respectively). The pDOS are shifted so that the Fermi level of the undecorated anatase  $\text{TiO}_2(101)$  surface is at 0 eV (shown as a vertical dotted black line) while maintaining the same vacuum energy for all systems (+5.7 eV here). We also indicate the energy of the top of the valence band and bottom of the conduction band of the undecorated  $\text{TiO}_2(101)$  using vertical green and blue dotted lines, respectively.

From the inspection of Figure 6a and b, we conclude that the electronic states of  $\text{TiO}_2(101)$  are altered only slightly (mostly due to rehybridization of occupied Ti orbitals) as a result of surface distortion needed to accommodate the cyclic  $(\text{MoO}_3)_3$  trimer. No shift of the valence or conduction bands is observed. In contrast, geometric distortion of  $(\text{MoO}_3)_3$  leads to the upward shift of its highest occupied molecular orbital (HOMO) to more closely align with  $\text{TiO}_2(101)$  pDOS. Comparison of Figure 6b and c shows that the surface does not experience any further electronic alteration due to adsorption of  $(\text{MoO}_3)_3$  apart from a slight downward shift ( $\sim 0.15$  eV) of the valence and conduction bands. However, significant changes in the  $(\text{MoO}_3)_3$  pDOS are seen upon adsorption, most notably the creation of three gap states within the bandgap of  $\text{TiO}_2(101)$ . Inspection of the orbitals in the relevant part of its wavefunction reveals that Mo 4d and O 2p empty states are most responsible for the topography of the simulated STM images shown in

Figure 3. We thus conclude that these gap states are centered on those orbitals. In fact, based on the area under Mo and O pDOS curve of each  $\text{MoO}_3$  in Figure 6c (cyan and magenta lines, respectively), we can conclude that the imaged orbitals are ~75% Mo 4d empty states and ~25% O 2p empty states. Inclusion of the single gap state that slightly overlaps the bottom of the  $\text{TiO}_2$  conduction band results in a breakdown of 66% from Mo 4d, 21% from  $(\text{MoO}_3)_3$  O 2p, 7% from Ti 3d, and 6% from  $\text{TiO}_2$  O 2p empty orbitals. Thus, the trimer gap states are dominated by Mo 4d states. Figure 6c and d show how the pDOS change upon the dissociation of cyclic  $(\text{MoO}_3)_3$  trimer into three  $(\text{MoO}_3)_1$  monomers (ATT used as an example). The  $\text{TiO}_2(101)$  surface remains electronically unchanged, but significant rehybridization of the orbitals in  $\text{MoO}_3$  is seen. Most notably, the three previous gap states coalesce into a single gap state containing 250% more states than before, with ~33% coming from Mo 4d and ~67% coming from O 2p empty states.

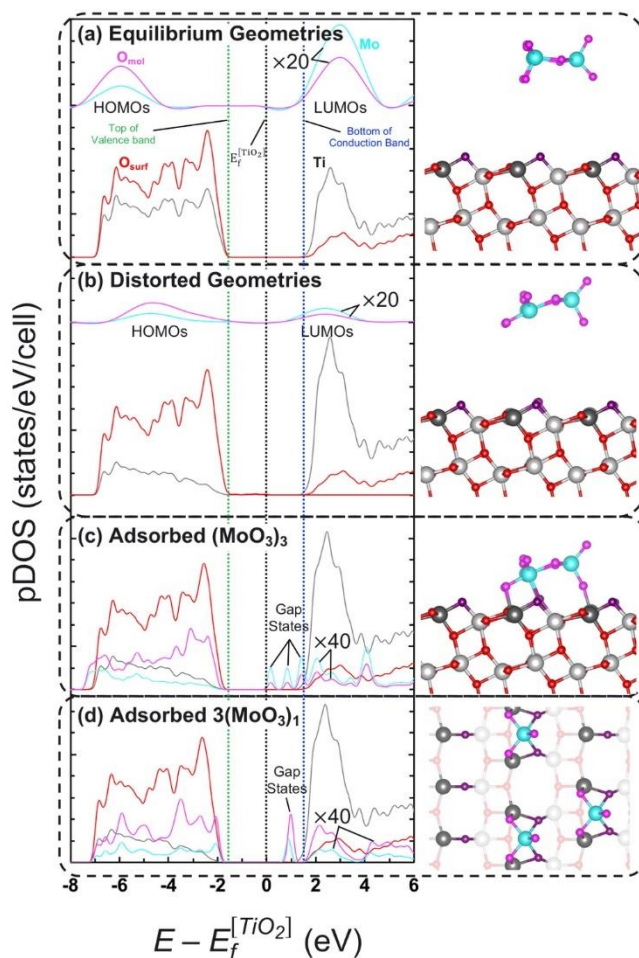


**Figure 6.** pDOS for different configurations of molybdenum trioxide on anatase  $\text{TiO}_2(101)$ . (a) Spatially separated  $(\text{MoO}_3)_3$  and bare  $\text{TiO}_2(101)$  in their equilibrium geometries. (b) Spatially separated  $(\text{MoO}_3)_3$  and bare  $\text{TiO}_2(101)$  in distorted geometries that are adopted after the adsorption. (c)  $(\text{MoO}_3)_3$  adsorbed on  $\text{TiO}_2(101)$  (see Figure 3a). No further geometric relaxation occurs from pDOS (b) to (c). (d) Three  $(\text{MoO}_3)_1$  monomers formed as a result of  $(\text{MoO}_3)_3$  dissociation on  $\text{TiO}_2(101)$  (see Figure 4a, structure ATT). Schematics on the right illustrate the configurations for calculated pDOS.

**The formation of ordered  $(\text{MoO}_3)_1$  overlayer.** We follow the progress of  $(\text{MoO}_3)_3$  adsorption and dissociation on the surface at higher coverages, STM images after the deposition of 0.10 and 0.17 ML of  $(\text{MoO}_3)_1$  equivalents are shown in Figure 7. As the coverage is increased to 0.10 ML (Figure 7a and b), the  $(\text{MoO}_3)_1$  monomers start to agglomerate into larger islands (several

highlighted by cyan ellipses, Figure 7b). These islands are frequently narrow, elongated along the  $[11\bar{1}]$  or  $[1\bar{1}\bar{1}]$  direction, and composed of a single chain of  $(\text{MoO}_3)_1$  (few highlighted by blue arrows, Figure 7a), but a few  $(\text{MoO}_3)_1$  trios (one ATT highlighted by a dotted magenta circle, Figure 7b) can still be recognized. The significant amount of clustering at this relatively low coverage is surprising and suggests that the gas phase molybdenum trioxide oligomers such as  $(\text{MoO}_3)_3$  and or the resulting  $(\text{MoO}_3)_1$  are mobile. The time-lapse sequences of STM images (not shown) demonstrate that the chemisorbed  $(\text{MoO}_3)_1$  do not diffuse, and the shape of the islands does not change with time. This suggests that clustering likely occurs transiently when the gas phase  $(\text{MoO}_3)_n$  clusters land on  $\text{TiO}_2(101)$ . Similar clustering has been observed on  $\text{TiO}_2(101)$  previously for water and methanol at 80 K.<sup>52-53</sup> There, we concluded that the molecules have to be mobile in some sort of precursor state before they chemisorb and become immobile at such low temperatures. The mobility of the intact  $(\text{MoO}_3)_n$  clusters upon landing is further supported by our statistical analysis displayed in Figure 7c. The quantitative comparison between the distribution of the cluster sizes at 0.03 ML (Figure 2a) and 0.10 ML (Figure 7c) shows that the percentage of  $(\text{MoO}_3)_1$  trios decreased dramatically while the percentage of the 2D  $\text{MoO}_3$  islands made of multiples of three units (i.e. with six, nine, twelve, etc.) increased noticeably and dominate the distribution. We take this as an evidence of cyclic  $(\text{MoO}_3)_3$  diffusion prior their dissociation into immobile  $(\text{MoO}_3)_1$  monomers. Further coverage increase to 0.17 ML (Figure 7d-e), demonstrates continued clustering and the formation of islands, always maintaining an elongated shape (a few of them are indicated by yellow arrows, Figure 7e) but no apparent long-range ordering is observed.

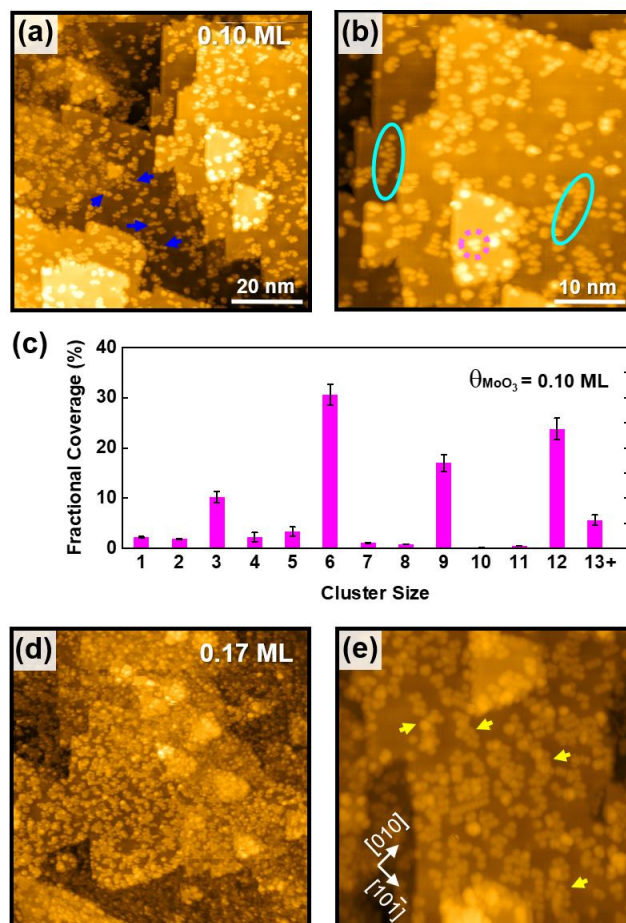


**Figure 7.** (a, d) Large-scale STM images (100 × 100 nm<sup>2</sup>,  $V_s = 1.9$  V,  $I_t = 40$  pA) of (a) 0.10 ML and (d) 0.17 ML of (MoO<sub>3</sub>)<sub>1</sub> deposited on TiO<sub>2</sub>(101) at 295 K. Blue arrows in (a) point to the individual MoO<sub>3</sub> chains. (b, e) Zoom in STM images (50 × 50 nm<sup>2</sup>,  $V_s = 1.5$  V,  $I_t = 50$  pA) of (b) 0.10 ML and (e) 0.17 ML of (MoO<sub>3</sub>)<sub>1</sub>. Magenta circle and cyan ellipses in (b) illustrate one of the isolated (MoO<sub>3</sub>)<sub>1</sub> trios and several (MoO<sub>3</sub>)<sub>1</sub> island, respectively. Yellow arrows in (e) mark the frequently observed elongated (MoO<sub>3</sub>)<sub>1</sub> islands. (c) Experimental distribution of the clustered (MoO<sub>3</sub>)<sub>1</sub> monomers on anatase TiO<sub>2</sub>(101) determined from the STM images after the deposition of 0.10 ML of (MoO<sub>3</sub>)<sub>1</sub> equivalents at 295 K.

The experimentally inferred immobility of (MoO<sub>3</sub>)<sub>1</sub> monomers can be further probed via DFT. As shown in Figure 8a, the reaction pathways for “along-row” (i.e., along the [010] direction) and “cross-row” (i.e. along the [11 $\bar{1}$ ] or [1 $\bar{1}$  $\bar{1}$ ] directions) diffusion are calculated to have the overall barriers of 83 and 188 kJ/mol/(MoO<sub>3</sub>)<sub>1</sub>, with the mechanism illustrated by the schematics in Figure 8b and c, respectively. While the cross-row barrier of 188 kJ/mol/(MoO<sub>3</sub>)<sub>1</sub> is extremely high and

not surmountable till very high temperature ( $\geq 614$  K), the along-row barrier should be accessible already upon a modest temperature increase ( $\geq 273$  K). The estimated temperatures are based on simple first order kinetics calculations to achieve experimentally observable diffusion rates ( $\sim 10^{-3}$  hops/s) with a standard prefactor of  $10^{13} \text{ s}^{-1}$ . Each diffusion path proceeds through two transitions states and contains a stable intermediate in the form of one of the two di-oxo  $(\text{MoO}_3)_1$  configurations shown in Figure S4a (for along-row) and Figure S4b (for cross-row) in the Supporting Information.

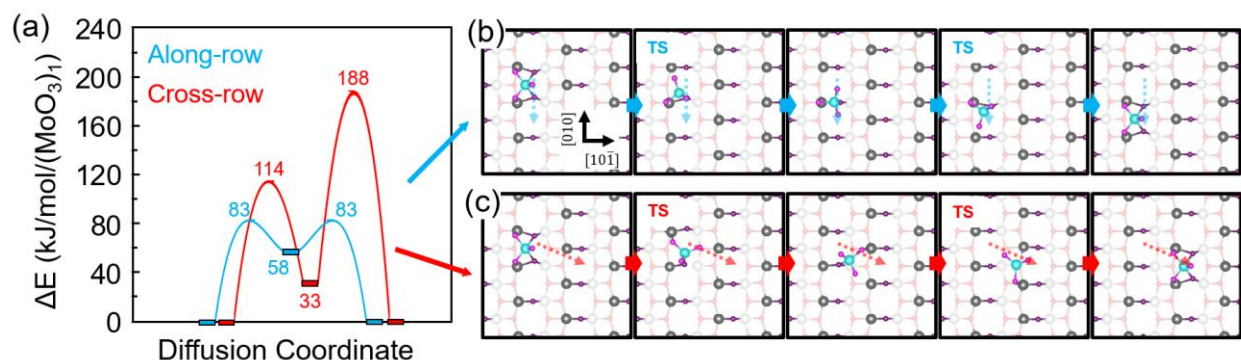


**Figure 8.** (a) Reaction pathways for along-row (blue) and cross-row (red) diffusion as determined from DFT/CINEB. The numerical values represent energy levels of each transition state and stable intermediate relative to the mono-oxo  $(\text{MoO}_3)_1$  configuration. Schematics in (b) and (c) show top views of the structures determined for (b) along-row and (c) cross-row (red) diffusion pathways. The initial configuration for  $(\text{MoO}_3)_1$  is identical with that shown in Figure 3c. Transitions states are labeled as TS and dashed arrows have been placed along each reaction path to guide the eye.

Further molybdenum trioxide dose to the coverage that approaches fully saturated first layer (0.5 ML) is shown in the STM images in Figure 9a and b. The  $(\text{MoO}_3)_1$  monomers are found to evenly cover the entire surface indicating that the deposited  $(\text{MoO}_3)_n$  clusters have to be mobile on the top of already deposited clusters that dissociated and bind as  $(\text{MoO}_3)_1$ . Such mobility allows for the completion of the first layer before the nucleation of the second layer is initiated. The high-magnification STM image (Figure 9b) further shows that locally the  $(\text{MoO}_3)_1$  monomers are arranged with a  $(2 \times 1)$  periodicity (blue parallelogram) forming nm-sized ordered domains. The



red and cyan lines indicate the positions of the representative line profiles that are displayed in Figure 9c. The line profiles demonstrate the average  $(\text{MoO}_3)_1 - (\text{MoO}_3)_1$  spacings of  $\sim 7.6$  and  $\sim 5.5$  Å along the  $[010]$  and  $[11\bar{1}]$  directions, respectively. This is in a good agreement with the periodicity expected for a  $(2\times 1)$  superstructure that is schematically displayed in Figure 9d. The simulated STM image for this configuration can be found in Section S5 of the Supporting Information. The adsorption energy of the 0.5 ML configuration in Figure 9d is calculated to be -180 kJ/mol/ $(\text{MoO}_3)_1$ . A comparison of the adsorption energy of -180 kJ/mol/ $(\text{MoO}_3)_1$  for the saturated surface (Figure 9d), with 197-192 kJ/mol for  $(\text{MoO}_3)_1$  trios (Figure 4a), and with -223 kJ/mol/ $(\text{MoO}_3)_1$  for isolated  $(\text{MoO}_3)_1$  (Figure 3c) clearly shows that the repulsive interactions are significant and lead to  $\sim 20\%$  reduction of the adsorption energy. Despite that, the interactions remain significantly stronger than the interactions between the molybdenum trioxide layers. Therefore, in the presence of low diffusion barrier of  $(\text{MoO}_3)_3$  on the top of  $(\text{MoO}_3)_1$  in the first layer, the formation of a full first layer is not that surprising.

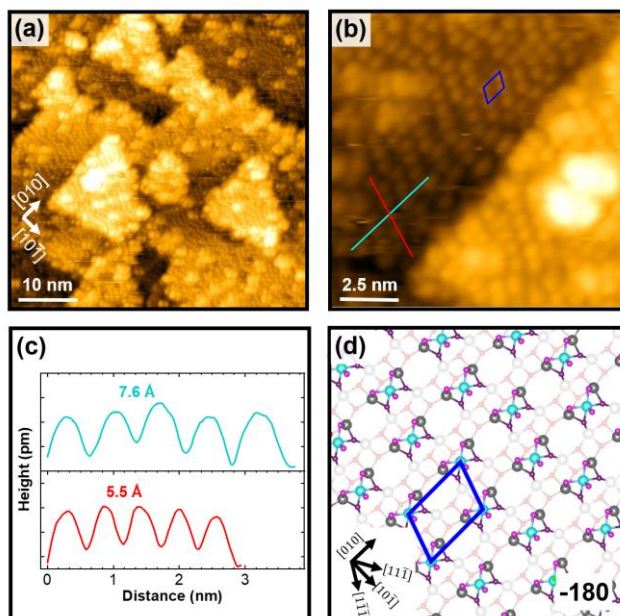


**Figure 9.** (a-b) STM images of  $\text{TiO}_2(101)$  after the deposition of saturation amount ( $\sim 0.5$  ML) of molybdenum trioxide at 295 K. Image conditions: (a)  $50 \times 50 \text{ nm}^2$ ,  $V_s = 1.4 \text{ V}$ ,  $I_t = 50 \text{ pA}$ , (b) 12.5



$\times 12.5 \text{ nm}^2$ ,  $V_s = +1.1 \text{ V}$ ,  $I_t = 60 \text{ pA}$ . The  $(2\times 1)$  unit cell of locally ordered structure is illustrated with blue parallelogram. (c) Line profiles taken along the directions indicated in (b). (d) Structural model of the  $(2\times 1)$  overlayer (blue parallelogram) of  $(\text{MoO}_3)_1$  monomers on  $\text{TiO}_2(101)$ , with calculated adsorption energy of  $-180 \text{ kJ/mol}/(\text{MoO}_3)_1$ . Coloring scheme in panel (d) is identical to that used in Figure 3.

---

**Thermal stability of the  $(\text{MoO}_3)_1$  overlayers.** In this section we follow the  $(\text{MoO}_3)_1$  monomers on  $\text{TiO}_2(101)$  as a function of annealing temperature to determine their stability towards reduction and diffusion into the  $\text{TiO}_2$  bulk. Selected STM images for 0.04 ML of  $(\text{MoO}_3)_1$  equivalents deposited at 295 K and subsequently annealed at 450, 550, and 650 K are shown in Figure 10. The as-prepared sample (Figure 10a) shows the typical distribution of  $(\text{MoO}_3)_1$  monomers as discussed in the previous sections.

The images obtained after annealing to 450 K (Figure 10b) show only subtle changes in the morphology and the distribution of  $(\text{MoO}_3)_1$ . The statistical analysis shows that the distribution after annealing to 450 K is similar to that before annealing (Figure 2a). This provides further evidence that once the gas phase  $(\text{MoO}_3)_n$  clusters dissociate and form  $(\text{MoO}_3)_1$  monomers they become immobilized. It also suggests that the *effective*  $(\text{MoO}_3)_1$  diffusion barrier is higher than the calculated value of  $83 \text{ kJ/mol}$  (Figure 8) since this would suggest observable diffusion above  $\sim 273 \text{ K}$ .

Further annealing at 550 K induces pronounced changes in the surface morphology, as shown in Figure 10c. A broader distribution of non-uniform bright features with different sizes and heights can be observed but some similarities with the distribution at 295 K (Figure 10a) is retained. Additionally, the density of bright spots decreased slightly, by  $\sim 18\%$ . These changes suggest structural changes of the  $(\text{MoO}_3)_1$  and some level of coalescence. The trend continues after annealing at 650 K (Figure 10d) where even bigger bright features (black dotted circle) appear. At

higher  $(\text{MoO}_3)_1$  coverages, analogous annealing-dependent behavior is observed (see Section S7, Supplementary Information).

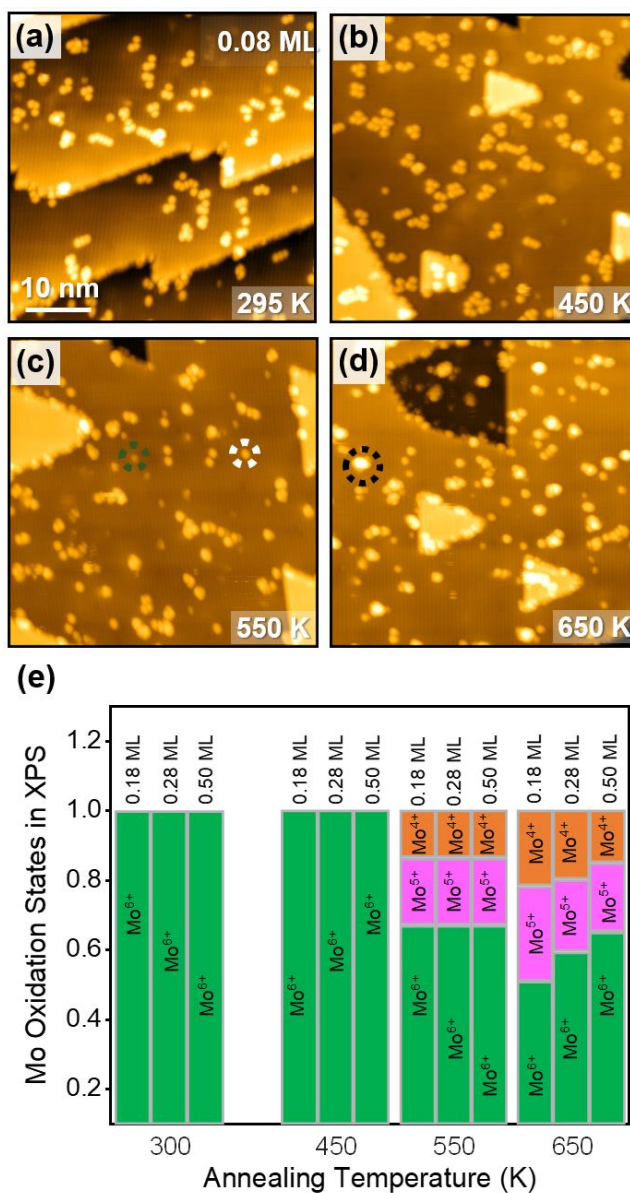


**Figure 10.** (a–d) STM images ( $45 \text{ nm} \times 45 \text{ nm}$ ,  $V_s = 1.5 \text{ V}$ ,  $I_t = 50 \text{ pA}$ ) of  $0.04 \text{ ML } (\text{MoO}_3)_3$  deposited on  $\text{TiO}_2(101)$  at  $295 \text{ K}$  (a) and subsequently annealed in UHV at (b)  $450 \text{ K}$ , (c)  $550 \text{ K}$ , and (d)  $650 \text{ K}$ . (e) The relative distributions of Mo oxidation states for  $(\text{MoO}_3)_1/\text{TiO}_2(101)$  determined from XPS Mo 3d spectra (see Section S8, Supporting Information).

Complementary information about the chemical state of the molybdenum trioxide on the  $\text{TiO}_2(101)$  was obtained from the XPS measurements as a function of the coverage and annealing

temperature (Figure 10b). A set of annealing temperature-dependent Mo 3d core-level spectra acquired for  $\sim 0.09$  ML of  $(\text{MoO}_3)_1$  equivalents with the details of the analysis are described in Section S8 of the Supporting Information section. As already discussed with Figure 2, the spectrum for as-prepared  $(\text{MoO}_3)_1$  monomers, can be fit by a single spin-orbit doublet that corresponds to Mo in (6+) oxidation state (Mo  $3d_{5/2}$  at 232.3 eV).<sup>2, 54</sup> This is true for all measured coverages shown in Figure 10b and no changes are observed upon annealing to 450 K. After annealing to 550 K, the Mo 3d spectra reveal an onset of reduction with 9% and 6% contributions from (5+) and (4+) oxidation states at all coverages (observed at 231.0 and 229.6 eV), respectively.<sup>53-54</sup> Further reduction is observed after annealing at 650 K and the extent being slightly higher at low coverages. Interestingly, despite the observed reduction, the annealing did not lead to a decrease in the overall Mo coverage on the surface. The changes observed in the XPS correlate well with the annealing-dependent STM images discussed above (Figure 10a-d and Figure S7), where Mo shows a tendency toward reduction to the lower oxidation states as the temperature is increased above 450 K.

The structural stability is also reflected in the energetics for the removal of an oxygen atom from  $(\text{MoO}_3)_1$ , which was determined by DFT. Starting from  $(\text{MoO}_3)_1$ , the activation barrier for the formation of  $(\text{MoO}_2)_1$  and a co-adsorbed O atom (bound to  $\text{Ti}_{5c}$ ) was calculated to be  $\sim 144$  kJ/mol with an endothermicity of 83 kJ/mol. Interestingly, this result suggests that the reduction of titania-supported  $(\text{MoO}_3)_1$  is kinetically and energetically hindered while it is likely favored entropically (1 mol going to 2 mol).

### 3. SUMMARY

In summary, we have synthesized highly-ordered overlayers of  $(\text{MoO}_3)_1$  monomers on anatase  $\text{TiO}_2(101)$  at 295 K by depositing the  $(\text{MoO}_3)_n$  oligomers from the gas phase. We have shown

previously that such oligomers where  $(\text{MoO}_3)_3$  is the dominant species can be prepared via a simple thermal sublimation of  $\text{MoO}_3$  powders. Here, a combination of high-resolution imaging via STM, spectroscopic analysis by XPS, and deposited mass measurements using QCM with theoretical studies via AIMD and DFT is employed to follow the deposition and dissociation as a function of coverage and temperature.

At low coverages, we find groupings of the  $(\text{MoO}_3)_1$  monomers on the surface that reflect the distribution of deposited  $(\text{MoO}_3)_n$  oligomers. Repeated imaging demonstrates that the  $(\text{MoO}_3)_1$  monomers are immobile at 295 K. For groupings of three  $(\text{MoO}_3)_1$  that originate from dominant  $(\text{MoO}_3)_3$  oligomer, detailed STM analysis shows four distinct equally populated configurations that span at least two  $\text{Ti}_{5c}$  rows. Notably, the configuration of three  $(\text{MoO}_3)_1$  on the same row is missing, indicating that the initial ring opening step occurs across two Ti rows. This is confirmed by AIMD simulations and DFT calculations, which further reveal that the  $(\text{MoO}_3)_1$  monomers are thermodynamically preferred over the cyclic  $(\text{MoO}_3)_3$  oligomer. In the most stable configuration, each  $(\text{MoO}_3)_1$  monomer is bound with two O atoms to neighboring  $\text{Ti}_{5c}$  sites and with Mo to two  $\text{O}_{2c}$  sites, leaving one  $\text{Mo}=\text{O}$  pointing into the vacuum.

At intermediate coverages, the size of the groupings increasing, and cross-row elongated islands are seen. This is taken as an evidence of the transient mobility of the  $(\text{MoO}_3)_n$  oligomers before their dissociation.

Finally, a saturation surface layer of  $(\text{MoO}_3)_1$  monomers with local  $(2\times 1)$  order can be formed indicating facile diffusion also on top of already  $(\text{MoO}_3)_1$  covered areas. Energetically, the adsorption energy of the monomers decreases with increasing coverage from  $-223$  kJ/mol to  $180$  kJ/mol due to electrostatic interactions.

Annealing depend studies reveal that at all coverages, the overlayers are stable to 450 K, with all Mo in (6+) oxidation state. Starting from 550 K, a fraction of the  $(\text{MoO}_3)_1$  becomes reduced to (5+) and (4+) oxidation state and the reduction continues as the temperature is increased further. Commensurate with the reduction, STM images reveal progressively higher levels of disordering in the  $(\text{MoO}_3)_1$  overlayers.

Overall, we have revealed the intricate mechanism of the interaction of the oligomeric  $(\text{MoO}_3)_n$  clusters with  $\text{TiO}_2(101)$  and dissociation into monomeric  $(\text{MoO}_3)_1$  units that can completely fill the surface. We find that large surface deformations are required to lower the energy of transition states during the decomposition indicating the importance of collective surface dynamics in the cluster decomposition kinetics. This is most apparent in the first Mo-O bond breaking event which forces the formation of Mo-O-Ti bonds to have a cross row geometry and limit the ability of the material to form LAT configurations upon further decomposition. The transient mobility of the oligomers on the surface is found to be responsible for the formation of the complete, locally ordered layer. These observations point to the critical role of surface templating in the formation and growth of these materials and can serve as guide to synthesize of other hierarchical oxide materials.

## 4. METHODS

**Experimental Details.** The experiments were performed in a commercial UHV system (Omicron), which is equipped with variable-temperature scanning tunneling microscopy (VT-STM), a dual x-ray source for Mg  $K\alpha$  and Al  $K\alpha$  radiation and a hemispherical electron analyzer (Omicron, EA125). The system comprises two separate chambers pumped by a combination of three turbomolecular pumps, one titanium sublimation pump, and one ion pump, resulting in a base pressure of  $\leq 7 \times 10^{-11}$  Torr. The anatase  $\text{TiO}_2(101)$  sample employed in this study is a natural

mineral crystal ( $5 \times 3 \times 1 \text{ mm}^3$ ), oriented and polished. The sample was mounted on a standard Omicron tantalum sample plate via thin tantalum foil clips and heated using a pyrolytic boron nitride (PBN) heater on the manipulator. The sample temperature was measured using a Type K thermocouple attached to the manipulator heating stage. The absolute temperature of the sample was checked with an infrared pyrometer (Heitronics, model KT19.81 II, 8-10  $\mu\text{m}$ ) and was found to be identical within  $\pm 15 \text{ K}$  to that measured by the thermocouple at all temperatures. Well-ordered  $\text{TiO}_2(101)$  (judged by STM and XPS) was prepared by repeated cycles of  $\text{Ne}^+$  ion sputtering at 295 K, and UHV annealing at 930 K. All STM images were recorded at 295 K in constant current mode (using electrochemically etched tungsten tips) at a positive sample bias in the range 0.7 to 2.2 V and with feedback currents between 30 and 90 pA. In the XPS measurements, Al  $K\alpha$  radiation has been used to excite Mo 3d, Ti 2p, and O 1s. A Shirley background was subtracted from all core level spectra. The Mo 3d core-level spectra have been decomposed into several components, whose individual shape consists of a Donjach-Šunjić profile convoluted with a Gaussian distribution.<sup>56</sup>

The Mo oxide overlayer has been prepared by the deposition of  $(\text{MoO}_3)_3$  clusters in UHV onto the clean  $\text{TiO}_2(101)$  surface held at 295 K. The  $(\text{MoO}_3)_3$  cluster beam has been generated by thermal sublimation of  $\text{MoO}_3$  powder at 830 K in a thermal evaporator (CreaTec); the evaporation flux ( $0.2\text{--}1.1 \text{ ngs}^{-1}\text{cm}^{-2}$ ) was monitored with a water-cooled quartz crystal microbalance (Inficon). The surface overage molybdenum oxide is given in monolayers (ML), where 1 ML is defined relative to the number of surface  $\text{Ti}_{5c}$  ions of  $5.17 \times 10^{14} \text{ cm}^{-2}$ .

**Computational Details.** We utilized the CP2K electronic structure package (version 6.1)<sup>57</sup> to perform unrestricted Kohn-Sham calculations of  $(\text{MoO}_3)_3$  clusters on Anatase  $\text{TiO}_2(101)$  surface. The modified Perdew-Burke-Ernzerhof (PBE)<sup>58-59</sup> exchange-correlation functional for solids

(PBEsol),<sup>60</sup> along with D3 type dispersion correction<sup>61</sup> (with a cutoff of 15 Å) was employed to model the system. Geodecker-Tetter-Hutter (GTH)<sup>62</sup> norm-conserving pseudopotentials were applied for description of the core electrons and the nuclei. For all elements present, double- $\zeta$  Gaussian MOLOPT basis sets<sup>63</sup> were used to describe the electrons, along with a plane wave cutoff of 400 Ry, in a gaussian – plane wave hybrid basis set scheme. The GGA+U scheme with a Hubbard parameter (U-J) of 8 eV for the Ti 3*d* states.<sup>64</sup> This results in a bulk anatase TiO<sub>2</sub> work function of 5.1 eV, which agrees well with that obtained from photoemission electron microscopy experiments reported by Xiong et al.<sup>65</sup> While many studies that use other quantum chemical packages typically employ a much lower Hubbard parameter, a larger value is required here due to our use of Mullikan charges to assess the populations needed to implement the GGA+U scheme within CP2K (differing from the method used in plane wave codes). Lastly, we also implemented a correction along the z-axis to rectify the surface dipoles due to the asymmetry of the slab surface. Brillion Zone integration is performed within the  $\Gamma$ -Point approximation, which is adequate due to the very large simulations cells used here. Further details concerning our computational methods can be found in Section S9 of the Supporting Information. All structural info for the computational models found in this work can be likewise be found in Section S10.

## ASSOCIATED CONTENT

**Supporting Information.** Section S1, Photoelectron spectroscopy of Mo-oxide clusters on anatase  $\text{TiO}_2(101)$  surface; Section S2, Determination of the amount of deposited molybdenum trioxide on  $\text{TiO}_2(101)$  via angle dependent XPS; Section S3, Stable binding configurations of cyclic  $(\text{MoO}_3)_3$ ; Section S4, Stable binding configurations of monomeric  $(\text{MoO}_3)_1$ ; Section S5, Simulated STM images for ATT and full monolayer configuration of  $(\text{MoO}_3)_1$  monomers; Section S6, AIMD Data for Decomposition of Cyclic  $(\text{MoO}_3)_3$ ; Section S7, STM images of molybdenum trioxide on  $\text{TiO}_2(101)$  as a function of coverage and annealing temperature; Section S8, XPS spectra of molybdenum trioxide on  $\text{TiO}_2(101)$  as a function of annealing temperature; Section S9, Further Computational Method Details; Section S10, Structural Data.

## ACKNOWLEDGMENT

This work was supported by the U.S. Department of Energy, Office of Science, Basic Energy Sciences, Chemical Sciences, Geosciences, and Biosciences Division. Experiments were performed in EMSL, a national scientific user facility sponsored by the Department of Energy's Office of Biological and Environmental Research and located at Pacific Northwest National Laboratory (PNNL). PNNL is a multiprogram national laboratory operated for DOE by Battelle. under Contract DE-AC05-76RL01830. Computational Resources were provided by a user proposal at the National Energy Research Scientific Computing Center (NERSC) located at Lawrence Berkley National Laboratory (LBNL).



## References

1. Poizot, P.; Laruelle, S.; Grugeon, S.; Dupont, L.; Tarascon, J. M., Nano-sized transition-metal oxides as negative-electrode materials for lithium-ion batteries. *Nature* **2000**, *407*, 496-499.
2. Rousseau, R.; Dixon, D. A.; Kay, B. D.; Dohnalek, Z., Dehydration, dehydrogenation, and condensation of alcohols on supported oxide catalysts based on cyclic  $(\text{WO}_3)_3$  and  $(\text{MoO}_3)_3$  clusters. *Chem. Soc. Rev.* **2014**, *43*, 7664-7680.
3. Wang, X.; Zhao, B.; Jiang, D.-e.; Xie, Y., Monolayer dispersion of  $\text{MoO}_3$ ,  $\text{NiO}$  and their precursors on  $\gamma\text{-Al}_2\text{O}_3$ . *Appl. Catal. A* **1999**, *188*, 201-209.
4. Li, Z.; Gao, L.; Zheng, S., Investigation of the dispersion of  $\text{MoO}_3$  onto the support of mesoporous silica MCM-41. *Appl. Catal. A* **2002**, *236*, 163-171.
5. Xiao, F.-S.; Zheng, S.; Sun, J.; Yu, R.; Qiu, S.; Xu, R., Dispersion of Inorganic Salts into Zeolites and Their Pore Modification. *J. Catal.* **1998**, *176*, 474-487.
6. Arnarson, L.; Rasmussen, S. B.; Falsig, H.; Lauritsen, J. V.; Moses, P. G., Coexistence of Square Pyramidal Structures of Oxo Vanadium (+5) and (+4) Species Over Low-Coverage  $\text{VO}_x/\text{TiO}_2$  (101) and (001) Anatase Catalysts. *J. Phys. Chem. C* **2015**, *119*, 23445-23452.
7. Zhou, G.; Zhao, T.; Qian, R.; Xia, X.; Dai, S.; Alsaedi, A.; Hayat, T.; Pan, J. H., Decorating (001) dominant anatase  $\text{TiO}_2$  nanoflakes array with uniform  $\text{WO}_3$  clusters for enhanced photoelectrochemical water decontamination. *Catal. Today* **2019**, *335*, 365-371.
8. Li, S.-C.; Li, Z.; Zhang, Z.; Kay, B. D.; Rousseau, R.; Dohnalek, Z., Preparation, Characterization, and Catalytic Properties of Tungsten Trioxide Cyclic Trimers on  $\text{FeO}(111)/\text{Pt}(111)$ . *J. Phys. Chem. C* **2012**, *116*, 908-916.
9. Mann, S.; Ozin, G. A., Synthesis of inorganic materials with complex form. *Nature* **1996**, *382*, 313-318.

10. Wintzheimer, S.; Granath, T.; Oppmann, M.; Kister, T.; Thai, T.; Kraus, T.; Vogel, N.; Mandel, K., Supraparticles: Functionality from Uniform Structural Motifs. *ACS Nano* **2018**, *12*, 5093-5120.
11. Lee, J.-H.; Koh, C. Y.; Singer, J. P.; Jeon, S.-J.; Maldovan, M.; Stein, O.; Thomas, E. L., 25th Anniversary Article: Ordered Polymer Structures for the Engineering of Photons and Phonons. *Adv. Mater.* **2014**, *26*, 532-569.
12. Gomez, I. J.; Arnaiz, B.; Cacioppo, M.; Arcudi, F.; Prato, M., Nitrogen-doped carbon nanodots for bioimaging and delivery of paclitaxel. *J. Mater. Chem. B* **2018**, *6*, 5540-5548.
13. Munnik, P.; de Jongh, P. E.; de Jong, K. P., Recent Developments in the Synthesis of Supported Catalysts. *Chem. Rev.* **2015**, *115*, 6687-6718.
14. Jaegers, N. R.; Lai, J.-K.; He, Y.; Walter, E.; Dixon, D. A.; Vasiliu, M.; Chen, Y.; Wang, C.; Hu, M. Y.; Mueller, K. T., *et al.*, Mechanism by which Tungsten Oxide Promotes the Activity of Supported V<sub>2</sub>O<sub>5</sub>/TiO<sub>2</sub> Catalysts for NO<sub>x</sub> Abatement: Structural Effects Revealed by 51V MAS NMR Spectroscopy. *Angew. Chem., Int. Ed.* **2019**, *58*, 12609-12616.
15. Diebold, U., The Surface Science of Titanium Dioxide. *Surf. Sci. Rep.* **2003**, *48*, 53-229.
16. Schoiswohl, J.; Sock, M.; Chen, Q.; Thornton, G.; Kresse, G.; Ramsey, M. G.; Surnev, S.; Netzer, F. P., Metal supported oxide nanostructures: model systems for advanced catalysis. *Top. Catal.* **2007**, *46*, 137-149.
17. Kim, Y. K.; Rousseau, R.; Kay, B. D.; White, J. M.; Dohnalek, Z., Catalytic dehydration of 2-propanol on (WO<sub>3</sub>)<sub>3</sub> clusters on TiO<sub>2</sub>(110). *J. Am. Chem. Soc.* **2008**, *130*, 5059-+.
18. Valden, M.; Lai, X.; Goodman, D. W., Onset of Catalytic Activity of Gold Clusters on Titania With the Appearance of Nonmetallic Properties. *Science* **1998**, *281*, 1647-1650.

19. Vajda, S.; White, M. G., Catalysis Applications of Size-Selected Cluster Deposition. *ACS Catal.* **2015**, *5*, 7152-7176.
20. Arnarson, L.; Falsig, H.; Rasmussen, S. B.; Lauritsen, J. V.; Moses, P. G., A complete reaction mechanism for standard and fast selective catalytic reduction of nitrogen oxides on low coverage VO<sub>x</sub>/TiO<sub>2</sub>(001) catalysts. *J. Catal.* **2017**, *346*, 188-197.
21. Henderson, M. A., A Surface Science Perspective on TiO<sub>2</sub> Photocatalysis. *Surf. Sci. Rep.* **2011**, *66*, 185-297.
22. Fujishima, A.; Rao, T. N.; Tryk, D. A., Titanium Dioxide Photocatalysis. *J. Photochem. Photobiol., C* **2000**, *1*, 1-21.
23. Elder, S. H.; Cot, F. M.; Su, Y.; Heald, S. M.; Tyryshkin, A. M.; Bowman, M. K.; Gao, Y.; Joly, A. G.; Balmer, M. L.; Kolwaite, A. C., *et al.*, The Discovery and Study of Nanocrystalline TiO<sub>2</sub>-(MoO<sub>3</sub>) Core–Shell Materials. *J. Am. Chem. Soc.* **2000**, *122*, 5138-5146.
24. Song, K. Y.; Park, M. K.; Kwon, Y. T.; Lee, H. W.; Chung, W. J.; Lee, W. I., Preparation of Transparent Particulate MoO<sub>3</sub>/TiO<sub>2</sub> and WO<sub>3</sub>/TiO<sub>2</sub> Films and Their Photocatalytic Properties. *Chem. Mater.* **2001**, *13*, 2349-2355.
25. Kong, F.; Huang, L.; Luo, L.; Chu, S.; Wang, Y.; Zou, Z., Synthesis and Characterization of Visible Light Driven Mesoporous Nano-Photocatalyst MoO<sub>3</sub>/TiO<sub>2</sub>. *J. Nanosci. Nanotechnol.* **2012**, *12*, 1931-1937.
26. Sviridova, T. V.; Sadovskaya, L. Y.; Shchukina, E. M.; Logvinovich, A. S.; Shchukin, D. G.; Sviridov, D. V., Nanoengineered thin-film TiO<sub>2</sub>/h-MoO<sub>3</sub> photocatalysts capable to accumulate photoinduced charge. *J. Photochem. Photobiol., A* **2016**, *327*, 44-50.

27. Doudin, N.; Kuhness, D.; Blatnik, M.; Barcaro, G.; Negreiros, F. R.; Sementa, L. ; Fortunelli, A.; Surnev, S.; Netzer, F. P., Nanoscale Domain Structure and Defects in a 2-D WO<sub>3</sub> Layer on Pd(100). *J. Phys. Chem. C* **2016**, *120*, 28682- 28693.
28. Li, Z.; Smid, B.; Kim, Y. K.; Matolin, V.; Kay, B. D.; Rousseau, R.; Dohnalek, Z., Alcohol Dehydration on Monooxo W=O and Dioxo O=W=O Species. *J. Phys. Chem. Lett.* **2012**, *3*, 2168-2172.
29. Fang, Z.; Li, Z.; Kelley, M. S.; Kay, B. D.; Li, S.; Hennigan, J. M.; Rousseau, R.; Dohnalek, Z.; Dixon, D. A., Oxidation, Reduction, and Condensation of Alcohols over (MO<sub>3</sub>)<sub>3</sub> (M = Mo, W) Nanoclusters. *J. Phys. Chem. C* **2014**, *118*, 22620-22634.
30. Mamoru, A., The Oxidation Activity and Acid-base Properties of Mixed Oxide Catalysts Containing Titania. I. The TiO<sub>2</sub>–MoO<sub>3</sub> and TiO<sub>2</sub>–V<sub>2</sub>O<sub>5</sub> Systems. *Bull. Chem. Soc. Jpn.* **1976**, *49*, 1328-1334.
31. Akimoto, M.; Echigoya, E., Carrier effect in vapor-phase oxidation of butadiene over supported molybdena catalysts. *J. Catal.* **1973**, *29*, 191-199.
32. Lietti, L.; Nova, I.; Ramis, G.; Dall'Acqua, L.; Busca, G.; Giamello, E.; Forzatti, P.; Bregani, F., Characterization and Reactivity of V<sub>2</sub>O<sub>5</sub>–MoO<sub>3</sub>/TiO<sub>2</sub> De-NO<sub>x</sub> SCR Catalysts. *J. Catal.* **1999**, *187*, 419-435.
33. Panagiotou, G. D.; Petsi, T.; Bourikas, K.; Kalampounias, A. G.; Boghosian, S.; Kordulis, C.; Lycourghiotis, A., Interfacial Impregnation Chemistry in the Synthesis of Molybdenum Catalysts Supported on Titania. *J. Phys. Chem. C* **2010**, *114*, 11868-11879.
34. Kim, D. S.; Wachs, I. E.; Segawa, K., Molecular Structures and Reactivity of Supported Molybdenum Oxide Catalysts. *J. Catal.* **1994**, *149*, 268-277.

35. La Fontaine, C.; Yoboue, A.; Berrier, E.; Tougeri, A.; Villain, F.; Fonda, E.; Hamraoui, K.; Paul, J. F.; Cristol, S., Methanol conversion over TiO<sub>2</sub>-anatase supported oxomolybdate catalysts: an integrated operando – DFT modeling approach. *Phase Transit.* **2011**, *84*, 700-713.
36. Woods, M. P.; Mirkelamoglu, B.; Ozkan, U. S., Oxygen and Nitrous Oxide as Oxidants: Implications for Ethane Oxidative Dehydrogenation over Silica–Titania-Supported Molybdenum. *J. Phys. Chem. C* **2009**, *113*, 10112-10119.
37. Reddy, B. M.; Chowdhury, B.; Smirniotis, P. G., An XPS study of the dispersion of MoO<sub>3</sub> on TiO<sub>2</sub>–ZrO<sub>2</sub>, TiO<sub>2</sub>–SiO<sub>2</sub>, TiO<sub>2</sub>–Al<sub>2</sub>O<sub>3</sub>, SiO<sub>2</sub>–ZrO<sub>2</sub>, and SiO<sub>2</sub>–TiO<sub>2</sub>–ZrO<sub>2</sub> mixed oxides. *Appl. Catal. A* **2001**, *211*, 19-30.
38. Guesmi, H.; Gryboś, R.; Handzlik, J.; Tielens, F., Characterization of molybdenum monomeric oxide species supported on hydroxylated silica: a DFT study. *Phys. Chem. Chem. Phys.* **2014**, *16*, 18253-18260.
39. Handzlik, J.; Sautet, P., Structure of Isolated Molybdenum(VI) Oxide Species on  $\gamma$ -Alumina: A Periodic Density Functional Theory Study. *J. Phys. Chem. C* **2008**, *112*, 14456-14463.
40. Handzlik, J.; Sautet, P., Structure of Dimeric Molybdenum(VI) Oxide Species on  $\gamma$ -Alumina: A Periodic Density Functional Theory Study. *J. Phys. Chem. C* **2010**, *114*, 19406-19414.
41. Fievez, T.; Geerlings, P.; Weckhuysen, B. M.; De Proft, F., Using DFT in Search for Support Effects During Methanol Oxidation on Supported Molybdenum Oxides. *ChemPhysChem* **2011**, *12*, 3281-3290.
42. Tsilomelekis, G.; Boghosian, S., On the configuration, molecular structure and vibrational properties of MoO<sub>x</sub> sites on alumina, zirconia, titania and silica. *Catal. Sci. Technol.* **2013**, *3*, 1869-1888.

43. Hamraoui, K.; Cristol, S.; Payen, E.; Paul, J.-F., Computational Investigation of TiO<sub>2</sub>-Supported Isolated Oxomolybdenum Species. *J. Phys. Chem. C* **2007**, *111*, 3963-3972.
44. Hamraoui, K.; Cristol, S.; Payen, E.; Paul, J. F., Structure and reducibility of titania-supported monomeric and dimeric molybdenum oxide entities studied by DFT calculations. *J Mol. Struc.-Theochem* **2009**, *903*, 73-82.
45. Kim, H. Y.; Lee, H. M.; Pala, R. G. S.; Metiu, H., Oxidative Dehydrogenation of Methanol to Formaldehyde by Isolated Vanadium, Molybdenum, and Chromium Oxide Clusters Supported on Rutile TiO<sub>2</sub>(110). *J. Phys. Chem. C* **2009**, *113*, 16083-16093.
46. Li, Z.; Fang, Z.; Kelley, M. S.; Kay, B. D.; Rousseau, R.; Dohnalek, Z.; Dixon, D. A., Ethanol Conversion on Cyclic (MO<sub>3</sub>)<sub>3</sub>(M = Mo, W) Clusters. *J. Phys. Chem. C* **2014**, *118*, 4869-4877.
47. Gong, X.-Q.; Selloni, A.; Batzill, M.; Diebold, U., Steps on anatase TiO<sub>2</sub>(101). *Nat Mater* **2006**, *5*, 665-670.
48. Hebenstreit, W.; Ruzycki, N.; Herman, G. S.; Gao, Y.; Diebold, U., Scanning tunneling microscopy investigation of the TiO<sub>2</sub> anatase (101) surface. *Phys. Rev. B* **2000**, *62*, R16334-R16336.
49. He, Y.; Dulub, O.; Cheng, H.; Selloni, A.; Diebold, U., Evidence for the Predominance of Subsurface Defects on Reduced Anatase TiO<sub>2</sub>(101). *Phys. Rev. Lett.* **2009**, *102*, 106105.
50. Setvin, M.; Schmid, M.; Diebold, U., Aggregation and electronically induced migration of oxygen vacancies in TiO<sub>2</sub> anatase. *Phys. Rev. B* **2015**, *91*, 195403.
51. Treacy, J. P. W.; Hussain, H.; Torrelles, X.; Grinter, D. C.; Cabailh, G.; Bikondoa, O.; Nicklin, C.; Selcuk, S.; Selloni, A.; Lindsay, R., *et al.*, Geometric structure of anatase TiO<sub>2</sub>(101). *Phys. Rev. B* **2017**, *95*, 075416.

52. Dahal, A.; Dohnálek, Z., Formation of Metastable Water Chains on Anatase  $\text{TiO}_2(101)$ . *J. Phys. Chem. C* **2017**, *121*, 20413-20418.
53. Dahal, A.; Petrik, N. G.; Wu, Y.; Kimmel, G. A.; Gao, F.; Wang, Y.; Dohnálek, Z., Adsorption and Reaction of Methanol on Anatase  $\text{TiO}_2(101)$  Single Crystals and Faceted Nanoparticles. *J. Phys. Chem. C* **2019**, *123*, 24133-24145.
54. Greiner, M. T.; Chai, L.; Helander, M. G.; Tang, W.-M.; Lu, Z.-H., Metal/Metal-Oxide Interfaces: How Metal Contacts Affect the Work Function and Band Structure of  $\text{MoO}_3$ . *Adv. Funct. Mater.* **2013**, *23*, 215-226.
55. Greiner, M. T.; Chai, L.; Helander, M. G.; Tang, W.-M.; Lu, Z.-H., Transition Metal Oxide Work Functions: The Influence of Cation Oxidation State and Oxygen Vacancies. *Adv. Funct. Mater.* **2012**, *22*, 4557-4568.
56. Doniach, S.; Sunjic, M., Many-electron singularity in X-ray photoemission and X-ray line spectra from metals. *J. Phys. C*. **1970**, *3*, 285-291.
57. Hutter, J.; Iannuzzi, M.; Schiffmann, F.; VandeVondele, J., CP2K: atomistic simulations of condensed matter systems. *Wiley Interdiscip. Rev. Comput. Mol. Sci.* **2014**, *4*, 15-25.
58. Perdew, J.; Burke, K.; Ernzerhof, M., Generalized Gradient Approximation Made Simple. *Phys. Rev. Lett.* **1996**, *77*, 3865-3868.
59. Perdew, J. P.; Burke, K.; Ernzerhof, M., Generalized Gradient Approximation Made Simple [Phys. Rev. Lett. 77, 3865 (1996)]. *Phys. Rev. Lett.* **1997**, *78*, 1396-1396.
60. Perdew, J. P.; Ruzsinszky, A.; Csonka, G. I.; Vydrov, O. A.; Scuseria, G. E.; Constantin, L. A.; Zhou, X.; Burke, K., Restoring the Density-Gradient Expansion for Exchange in Solids and Surfaces. *Phys. Rev. Lett.* **2008**, *100*, 136406.

61. Grimme, S.; Antony, J.; Ehrlich, S.; Krieg, H., A consistent and accurate ab initio parametrization of density functional dispersion correction (DFT-D) for the 94 elements H-Pu. *J. Chem. Phys.* **2010**, *132*, 154104.
62. Goedecker, S.; Teter, M.; Hutter, J., Separable Dual-Space Gaussian Pseudopotentials. *Phys. Rev. B* **1996**, *54*, 1703-1710.
63. VandeVondele, J.; Hutter, J., Gaussian Basis Sets for Accurate Calculations on Molecular Systems in Gas and Condensed Phases. *J. Chem. Phys.* **2007**, *127*, 114105.
64. Dudarev, S. L.; Botton, G. A.; Savrasov, S. Y.; Humphreys, C. J.; Sutton, A. P., Electron-Energy-Loss Spectra and the Structural Stability of Nickel Oxide: An LSDA+U Study. *Phys. Rev. B* **1998**, *57*, 1505-1509.
65. Xiong, G.; Shao, R.; Droubay, T. C.; Joly, A. G.; Beck, K. M.; Chambers, S. A.; Hess, W. P., Photoemission Electron Microscopy of TiO<sub>2</sub> Anatase Films Embedded with Rutile Nanocrystals. *Adv. Funct. Mater.* **2007**, *17*, 2133-2138.



